Assessment of Melt Cleanliness of Secondary 5000 Aluminum Alloy *Via* Non-metallic Inclusions Characterization

CONG LI, MERTOL GÖKELMA, THIEN DANG, JINXIAN HUANG, CHUNFA HUANG, JIANGUO LI, and BERND FRIEDRICH

The extensive energy consumption of primary aluminum production stimulates increasing need of producing primary-quality alloys with secondary sources, during which process amount of non-metallic inclusions (NMIs) in the alloy must be strictly controlled. In the present study funded by AMAP Open Innovation Research Cluster, NMIs generated during remelting a 5000 Al-Mg alloy was investigated to offer benchmarking characters of NMIs with respect to type, morphology, size, composition, and concentration. Under different remelting conditions NMIs formed in the melt ahead of solidification were concentrated using Porous Disc Filtration Apparatus (PoDFA) and characterized microstructurally and quantitatively. Investigated conditions included heating cycle, organic contaminations, and refractory materials. Results suggested oxide films and cuboid particles as typical oxides with, respectively, different compositions. The amount of formed oxides declined with the increase of heating rate. With respect to aluminum carbide (Al_4C_3), organic contaminations were confirmed to lead to an increased amount of its formation. The carbon-containing refractory material contributed more significantly than organic contaminations on the formation of Al_4C_3 at melt temperatures over 760 °C. Formulas were derived based on trial results to enable translation of NMIs PoDFA value [mm^2/kg] into their mass fraction [ppm] in the melt.

I. INTRODUCTION AND MOTIVATIONS

THE pursuit of sustainable and decarbonizing development prompt rapid development of recycling,[1] during which process a great amount of alloys (*e.g.*, aluminum, steel alloy) are remelted to produce new products. Despite challenges, a favorable scenario is to use secondary sources to produce primary-quality alloys. During remelting, not only the alloy composition but also amount of harmful non-metallic inclusions (NMIs), *e.g.*, oxides and carbide should be strictly controlled since the presence of those inclusions will pose difficulties in subsequent metal working processes, dramatically deteriorate the surface quality, and negatively affect mechanical property of the final products.[2–5]

Monitoring of NMIs content along the process route plays a central role in controlling NMIs amount in final product. From steelmaking perspective of view, various NMIs characterization methods including microscopy,[6] emission spectroscopy,[7] fracture analysis,[8] oxygen analysis,[9] have been developed over decades. With respect to aluminum industry, most above mentioned methods except for oxygen analysis find suitable applications. Meanwhile methods based on electrical,[10,11] acoustical,[12,13] and chemical[14] principles have also been developed featured for measuring amount and size of NMIs directly in the melt or after casting. In the case of low incidence of NMIs, a forced concentration is necessary to ease microscopical analysis. For steel samples, electron beam button melting (EBBM) and cold crucible remelting (CCR) were two reported methods for NMIs concentration.[8] With regards to aluminium, Porous Disc Filtration Apparatus (PoDFA)

CONG LI and BERND FRIEDRICH are with the IME Process Metallurgy and Metal Recycling, RWTH Aachen University, 52056, Aachen, Germany. Contact e-mail: cli@ime-aachen.de MERTOL GÖKELMA is with the Department of Materials Science and Engineering, Izmir Institute of Technology, 35430, Izmir, Turkey. THIEN DANG is with the TRIMET Aluminium SE, 45356, Essen, Germany. JINXIAN HUANG was with the School of Materials Science and Engineering, Tsinghua University, 100084, Beijing, P.R. China and now with the Department of Materials Science, Tohoku University, 980-8579, Sendai, Japan. CHUNFA HUANG and JIANGUO LI are with the School of Materials Science and Engineering, Tsinghua University.

is the state of art set-up for doing so.[15] By pressurized filtration, inclusions are concentrated by 10,000 times. Followed by a metallographic and microscopical examination, a comprehensive NMIs picture within the melt with respect to size, morphology and chemistry can be depicted. However, the disadvantage of PoDFA method is that it can only deliver Quantitative Index values with a unit [mm^2/kg]. The result can be interpreted as the area of inclusions collected above the filter when a unit mass of melt passes the filter. The real mass fraction of inclusions in the melt is however not available *via* PoDFA analysis. The method to translate NMIs PoDFA value into their real mass fraction in the melt is very much experience based.[16]

Despite the above disadvantage, PoDFA has been widely used as a state of art method to characterize NMIs in both laboratories and industrial plants. Aluminum cast alloys were investigated for many times where the reference inclusion characters had been made available.[17–19] Nevertheless, a comprehensive study for characterizing NMIs existed in 5000 Al-Mg alloy is missing. As a technical important alloy, 5000 Al-Mg alloy is consumed at a constantly growing rate, leading to increasing pressure of recycling. However, little information is available in the literatures with respect to boundary conditions of NMIs under different (re)-melting conditions including difference heating cycles or different refractories used for melting.

On the other hand, as closely correlated research fields, the formation of NMIs (*e.g.*, oxides, carbide) has been extensively investigated in other scenarios and the results lie a sound basis for interpreting characterization results belong to presented study. Therefore, in the follow-up sub-chapters, the existing knowledge with regards to formation of oxides, carbide, and introduction of boride are reviewed. Motivation and overview pertaining to the presented study are given at end of Chapter I.

A. Oxides

Oxide is one of the most deleterious and pervasive inclusion types in Al-Mg melts.[3,20] They are generally formed by oxidative reactions due to high oxygen affinity of aluminum and magnesium.[21,22]

Thermodynamic calculations have been made to predict stable oxide products at varying concentrations of Mg. Table I summarizes detailed information about thermodynamically stable oxide at different temperatures and Mg concentrations.[23–25] It is commonly acknowledged, with Mg concentration lower than 0.1 wt pct, Al$_2$O$_3$ is the most stable oxidative product. In the range of 0.1 to 1.5 wt pct and > 1.5 wt pct Mg concentration, MgAl$_2$O$_4$ and MgO is, respectively, the most favorable oxidation product.

The oxidation behavior of Al-Mg alloys has been extensively studied. Table II offers a summary of literature results. The Mg concentration was similar to the alloys used in the current study. It can be seen that the oxidative products in practical cases often deviate from thermodynamic predictions. For instance in alloys with over 4 wt pct Mg, MgAl$_2$O$_4$ were often identified as oxidative product particularly at extended exposed time.[26–29] In lab-scale trials (Haginoya *et al.*[28]) where the charging was mostly in gram scale, the occurrence of MgAl$_2$O$_4$ could be attributed to Mg depletion in the base alloy. Nevertheless, in pilot- and industrial-scale trials (Das *et al.* and Wen *et al.*),[26,27] chargings were often in ton-scale, the identification of MgAl$_2$O$_4$ cannot be reasonably explained by depletion theory since Mg concentration of the melt did not change significantly within the heating cycle. In most of the tabulated oxidation studies, oxidative products analysis was performed to support kinetic study of metal loss. Only limited focus was put on characterizing oxide inclusions entrapped within the melt.[30] Not to mention their morphology, concentration and evolutions under different melting conditions.

B. Carbides

One of the origins of the aluminum carbide (Al$_4$C$_3$) formation is the contact between aluminum melt and carbon or carbonaceous species. At elevated temperatures, carbon (C) in contact with the melt first dissolves into the melt (*e.g.*, electrolysis cell). When the melt undergoes temperature decrease, carbon precipitates in the form of fine Al$_4$C$_3$ particles due to a notable decrease of carbon solubility.[35]

The carbide concentration in solidified metal as a function of melt process temperature were measured by and Dorward[35] and Rødseth *et al.*[36] The relations of Dorward and Rødseth are in good agreement in the range of 685 °C to 1100 °C and often seen as a benchmark. Gökelma *et al.*[37] studied the effect of remelting on Al$_4$C$_3$ concentration. Samples were taken at 700 °C, 750 °C, and 800 °C and most of the results showed lower concentration than the measurements of Dorward and Rødseth. All measurements in the literatures are compiled in Figure 1.

Liquid sample in gram scale is taken during the carbide concentration measurements *via* gas chromatography (GC) method.[38] The method provides sensible data for benchmarking the Al$_4$C$_3$ concentration in solid

Table I.   Thermodynamically Stable Oxide at Different Temperatures and Mg Concentrations[23–25]

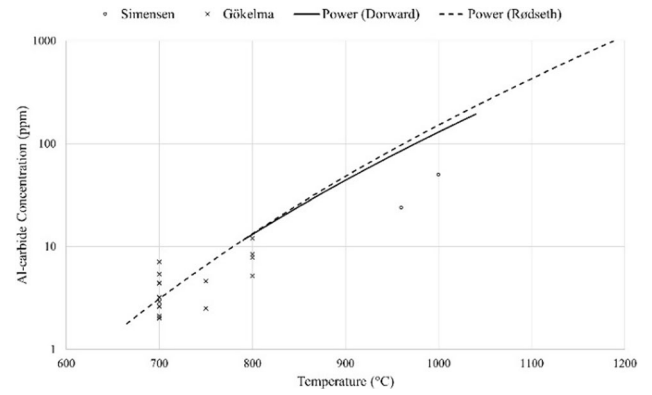| Temperature	Al$_2$O$_3$ Stable	MgAl$_2$O$_4$ Stable	MgO Stable
500 °C (solid)	0–0.14 wt pct Mg	0.14–0.93 wt pct Mg	> 0.93 wt pct Mg
700 °C (liquid)	0–0.058 wt pct Mg	0.058–2.17 wt pct Mg*	> 2.17 wt pct Mg
725 °C (liquid)	0–0.0089 wt pct Mg*	0.0089–1.34 wt pct Mg*	> 1.34 wt pct Mg
800 °C (liquid)	0–0.038 wt pct Mg	0.038–1.46 wt pct Mg	> 1.46 wt pct Mg

*Value estimated based on plot.

Fig. 1—Carbide concentration in solidified metal as a function of melt process temperature.[35–37,40,41]

metal under the assumption that C is fully dissolved in liquid metal. Nevertheless, for a more complex situation where Al_4C_3 particles pre-exists in the melt and are not distributed homogeneously,[39,40] the method finds its restriction due to limited sampling volume. In those cases, PoDFA method is a better option as it is capable to analyze samples with mass up to kilograms. However, the relation between PoDFA value and GC value of Al_4C_3 is yet to be established.

The organic contaminations *e.g.*, paint or grease of Al scraps were proposed to be another potential source for Al_4C_3 formation.[42] Despite several attempts were made on identification of Al_4C_3 during remelting of scraps with organic contaminations,[43,44] robust evidence is still missing to confirm formation of Al_4C_3 particles originated from organic contaminations. The difficulty lies possibly on low concentration of formed Al_4C_3 and its extremely high reactivity with moisture in air.[45]

C. Other Inclusions

Titanium diboride (TiB_2) is also, one of the typical NMIs, present in Al-Mg alloys. Unlike oxides and carbide which are formed by various reactions, TiB_2 is an inclusion deliberately introduced into the melt using grain refiner (*e.g.*, Al-5Ti-1B) master alloy for a purpose of refining grains.[46,47] During multiple rounds of recycling, boride particles can accumulate and their concentration in the melt needs to be closely monitored.[48] Similar to other inclusions, a sound way to translate boride PoDFA value into its mass fraction in the melt is yet to be established.

D. Overview of Completed Work

The completed study funded by AMAP Open Innovation Research Cluster intends to provide benchmarking characteristics of non-metallic inclusions (NMIs) in as-remelted 5000 Al-Mg alloy with respect to type, morphology, size, composition, and concentration. AA-5182 alloy was remelted at elevated temperatures. Afterwards a PoDFA set-up was employed to concentrate NMIs formed during alloy remelting and existed in advance of alloy solidification. The characterization

Table II. Oxidative Products of Al-Mg Alloys at Various Conditions[23,26–29,31–34]

Mg (wt pct)	Initial Surface Condition	Temp. (°C)	Time (hour)	Oxides*	Ref
4.2	electro-polished	400	1	MgO	Field et al.[31]
4.13	N.A	695	N.A	MgAl2O4	Das et al[26]
4.5	with organic coating	760–870	≤ 7	MgO & MgAl2O4 (short time); Al2O3 & MgAl2O4 (long time)	Wenz et al.[27]
4.0–5.0	N.A	500–800	≤ 72	MgO	Tenorio et al.[32]
4.39	melt in launder	N.A	N.A	Al2O3, MgO	Damoah et al[33]
5	skimmed melt	750	1	MgO	More et al[34]
1.3–9.3	as-cast	500–750	≤ 2	amorphous-MgO (short time); MgO (long time)	Silva et al.[23]
2–12.0	as-cast	650–900	≤ 3	MgO (short time); MgAl2O4 (long time)	Haginoya et al.[28]
1.0–14.0	as-cast	600–1100	100	MgO, MgAl2O4	Cochran et al[29]

*MgO and MgAl2O4 in crystalline form is implied without pre-fix.

results were presented respectively in sub-chapter-A to C of Chapter II. An overview of inclusion characteristics is given in sub-chapter D of Chapter II.

Influencing factors including heating cycle, organic contamination, and refractory material were studied with an aim to clarify the source of NMIs as well as deliver boundary conditions of common inclusions present in the melt. Formulas enabling translating NMIs PoDFA value [mm^2/kg] into their mass fraction [ppm] value were derived based on trial results. The effectiveness of formulas was demonstrated using boride particle as an example.

II. EXPERIMENTAL METHODOLOGY

A. Remelting of AA5182 Aluminum Alloy Sheets

AA5182 aluminum sheet [Figure 2(a)] was used to prepare a secondary 5000 aluminum alloy melt. Composition of the alloy is listed in Table III. Table IV gives the parameters of all trials and the corresponding characterization method.

The dimension of a single sheet was 115 × 65 × 2.8 mm. The sheet form was used due to its high specific surface area, which intensified the oxidation behavior and hence eased follow-up characterization work. Both as-received and degreased sheets were used in the trials (Table IV) to study the effect of organic contaminants on the formation of oxides and carbide. On the surface of as-received sheets, there were adhered organic residues composed of mainly cutting grease, rolling oil, and lubricants. The degreasing was performed by successive immersion, rinsing, and ultrasonic cleaning using commercial organic degreaser and demineralized water.

Both clay-graphite crucible [Figure 2(b)] and alumina-lined crucible [Figure 2(c)] with respectively ca. 2 L capacity were used for melting. The purpose of using two types of crucibles is to investigate the influence of refractory materials on the formation of carbide inclusions.

Remelting of ca. 2.2 kg alloy was carried out using a resistance heated furnace covered by insulating refractory with only an opening left for thermocouples. A K-type thermocouple shielded by alumina tube was positioned at middle of the crucible in contact with charged material in order to monitor the temperature variance during the course of melting and melt holding. The thermocouple was connected to a box equipped with MCPS temperature measurement system, which allowed for a record of temperature at a 0.1 second interval.

As is shown in Table IV, the alloy was melted at 720 °C, 760 °C, 800 °C and 840 °C. The respective temperature variance with time elapsed was measured and plotted in Figure 3. During 760 °C, 800 °C and 840 °C trials, alloy was charged into the crucible before onset of heating cycle (data from clay-graphite trials). The heating rate of the furnace was set at 10 °C per minute and the time including alloy heating, melting and melt holding was fixed at 4 hours. Particularly for 720 °C trials, alloy was charged into a crucible preheated at 720 °C.

Shortly before PoDFA sampling, the melt was moderately stirred to release inclusions that entrapped within dross layer into melt bath and meanwhile activate settled inclusions. Finally, the melt was transferred for a pressurized filtration via PoDFA.
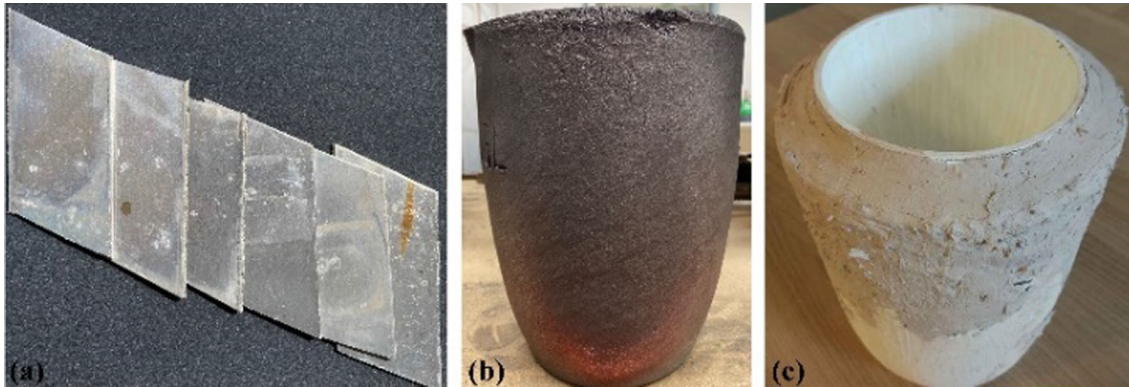
Fig. 2—Raw materials and crucibles: (a) AA-5182 sheet; (b) clay-graphite crucible; (c) alumina-lined crucible.

Table III. Chemical Composition of Investigated Alloy

AA-5182	Mg (Wt Pct)	Si (Wt Pct)	Ti (Wt Pct)	V (Wt Pct)	Al (Wt Pct)	B (Wt Pct)	Zr (Wt Pct)
As-received	4.72	0.082	0.015	0.011	bal.	0.0003	< 0.0003
Sample*	4.58	0.096	0.023	0.011	bal.	0.0019	< 0.0003

*Taken shortly before PoDFA measurement, given as an example result.

Table IV. Parameters of Designed Trials and Inclusion Characterization Method

Trial Number	Trimming Condition	Crucible	Temp.(°C)	PoDFA Analysis	SEM–EDS
1	as-received	clay-graphite	720	x	
2	ss-received	clay-graphite	720	x	
3	degreased	clay-graphite	720	x	
4	as-received	alumina	720	x	
5	degreased	alumina	720	x	
6	as-received	clay-graphite	760	x	x*1
7	as-received	clay-graphite	760	x	x*2
8	as-received	alumina	760	x	
9	as-received	clay-graphite	800	x	x*1
10	as-received	clay-graphite	800	x	x*2
11	degreased	clay-graphite	800	x	
12	as-received	alumina	800	x	
13	degreased	alumina	800	x	
14	as-received	clay-graphite	840	x	x*1
15	as-received	clay-graphite	840	x	x*2

*1: Sample prepared by electrochemical polishing.
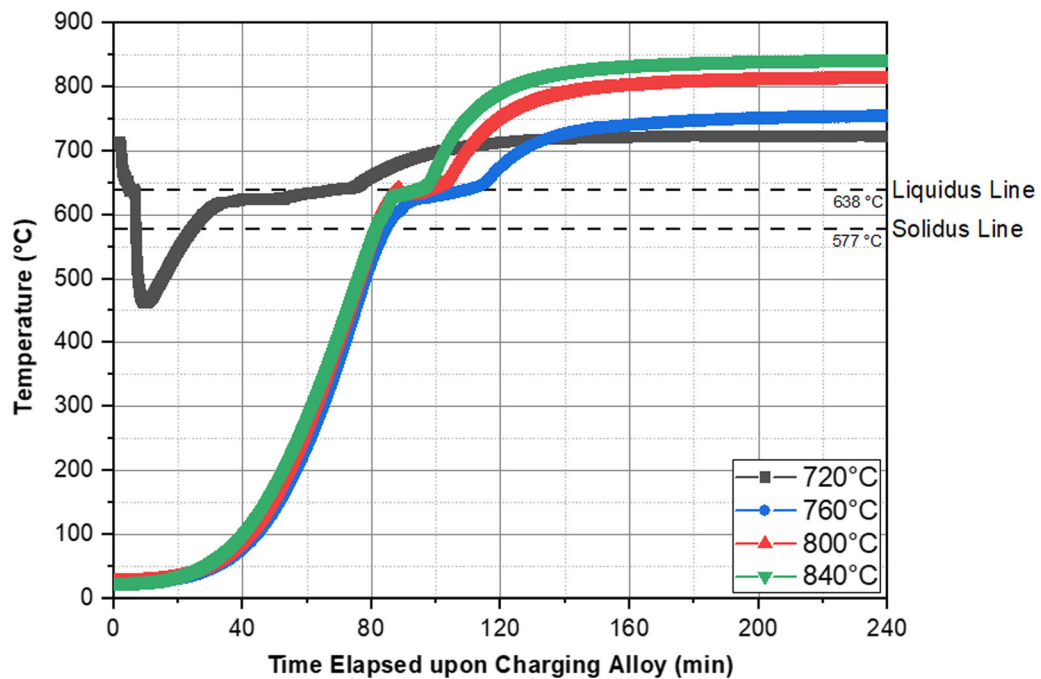*2: Sample prepared by mechanical polishing.

Fig. 3—Time-dependent temperature variance of alloy. Dashed lines indicate solidus and liquidus temperature of AA-5182 alloy.

B. Melt Filtration Via PoDFA

The principle of PoDFA method is schematically outlined in Figure 4. After the melt is transferred to a preheated crucible, the filtration starts by application of a negative pressure in the chamber below. As filtration progresses, the melt is forced to pass the porous filter disc, above which inclusions build up. At the end of the filtration, the negative pressure in the chamber is cancelled, after which unfiltered melt containing collected inclusions are allowed to solidify within the crucible.

A ~ 5 cm long metal sample containing inclusions along with filter disc was cut transversely from the entire solidified metal and sectioned longitudinally into two halves for follow-up metallographic preparation and microstructural examinations. The sectioning procedures as well as an optical micrograph of a polished sample are also shown in Figure 4.

C. Inclusion Counting and Microstructural Examination

One half of the PoDFA samples from each trial was mounted, ground and polished to mirror-like. After-
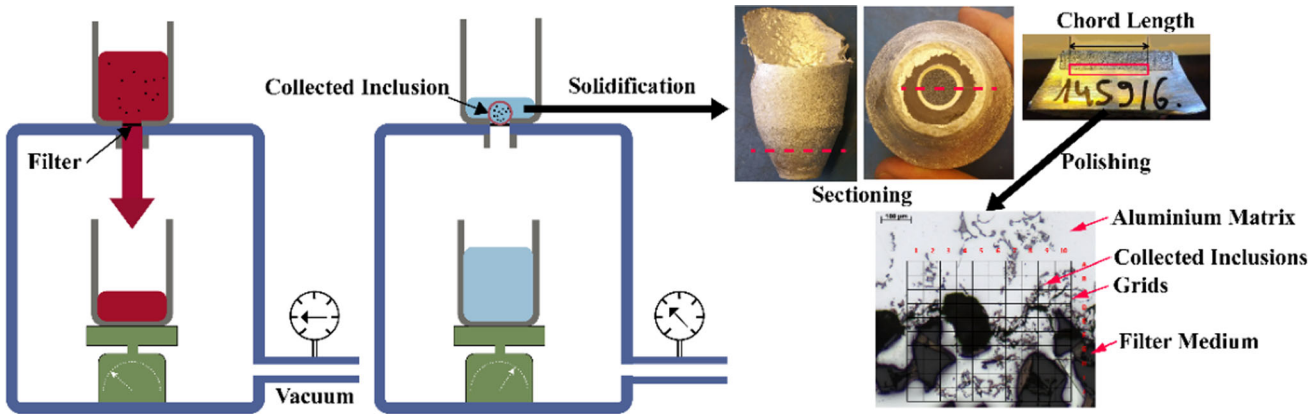
Fig. 4—Principle of Porous Disc Filtration Apparatus analysis including filtration, sample preparation, and inclusion counting. Elaborated based on Ref. [15,49].

wards the analyzing of non-metallic inclusions was performed at TRIMET R&D laboratory. During PoDFA counting, amount of specific inclusion type was calculated using below formula:

$$P_{inc} = \frac{A_{inc}}{m_{fil}} \cdot \frac{L_{noc}}{L_{mec}} \qquad [1]$$

where P_{inc} [mm²/kg] is defined PoDFA value of a specific inclusion type, A_{inc} [mm²] is area of collected inclusion above the filter which is counted *via* a grid method (Figure 4) proprietary to ABB Bomem. m_{fil} [kg] is mass of melt which pass the filter. L_{noc} [mm] is the nominal chord length (Figure 4) given by ABB and L_{mec} [mm] is the measured chord length in the analyzed sample.

For a detailed characterization of oxides in term of size, morphology and composition, one half of PoDFA samples from Trial Nr. 6, 9, 14 were selected for SEM–EDS analysis. The surface of selected samples was prepared by successively grinding until grade 2000 emery paper, after which it was electrochemically polished in a Desy and Hammer solution composed of perchloric acid ($HClO_4$) and ethyl alcohol.[50]

For identification of Al_4C_3, one half of PoDFA samples from Trial Nr. 7, 10, 15 were selected for in-situ SEM–EDS analysis. Given the easily hydrolyzed nature of Al_4C_3, the surface of selected samples was prepared by grinding using absolute ethanol as cooling liquid and afterwards mechanically polished using ethanol-based diamond suspension.

The inclusion counting was conducted with employment of ZEISS Optical Microscope (OM). The microstructural and elemental analysis of the inclusions were performed with a FEI QUANTA 200 FEG Scanning Electron Microscope (SEM), equipped with a backscattered electron detector and an EDAX energy dispersive X-Ray spectroscopy (EDS) facility, operating at an accelerating voltage of 15 to 20 kV. The in-situ observation of carbide degradation was carried out using HITACHI SU8200 SEM, equipped with a Bruker EDS facility, operating at an accelerating voltage of 5 to 10 kV.

III. RESULTS AND DISCUSSIONS

In this chapter, the results pertaining to oxides, carbide and boride are presented in sequence from sub-chapter III–A to III–C. A summary of inclusion characteristics is given in sub-chapter III-D.

A. Oxides

Microstructural examination of oxides in PoDFA samples from 760 °C, 800 °C, and 840 °C trial (Trial Nr. 6, 9, and 14) provides detailed information with regards to their morphology and composition. Figures 5(a) through (f) shows representative micrographs. Figure 5(a) gives an overview of NMIs generated at 800 °C. Above the filter medium, inclusions formed a cake layer where thick oxide films (marked by white arrows) can be readily distinguished. Close-up SEM observations suggest the presence of both oxide films and cuboid particles. Figures 5(b) through (d) shows representative micrographs of oxide films with different morphologies. Figure 5(e) shows a typical cuboid oxide particle. Note that electrochemical polish method offers a good distinguish of oxides with respect to alloy matrix and other inclusions, which helps to reveal morphology of different oxides and more importantly their evolution. Figure 5(f) shows an example that a particular oxide being in an intermedia status where cuboid particles nucleate upon an oxide film.

Dimension measurement conducted on samples from Trial Nr. 6, 9, 14 suggests oxide films have a length spanning from 15 to 200 μm and thickness ranging from 0.1 to 3 μm. Oxide particles in cuboid/polyhedral form [Figure 5(d)] have a size ranging from 0.5 to 3.0 μm. A detailed oxide inclusion size distribution will be presented in sub-chapter III-D.

Randomly picked oxides over the chord length were analyzed in composition using samples from 760 °C and 840 °C trial (Trial Nr. 6 and 14). The Mg, Al, and O wt pct of each oxide were plotted in a ternary diagram given in Figure 6(a). Since oxide films are mostly thinner than 2 μm, EDS results unavoidably included contribution of alloy matrix. In order to remove the "background" signal, the oxide elemental composition was
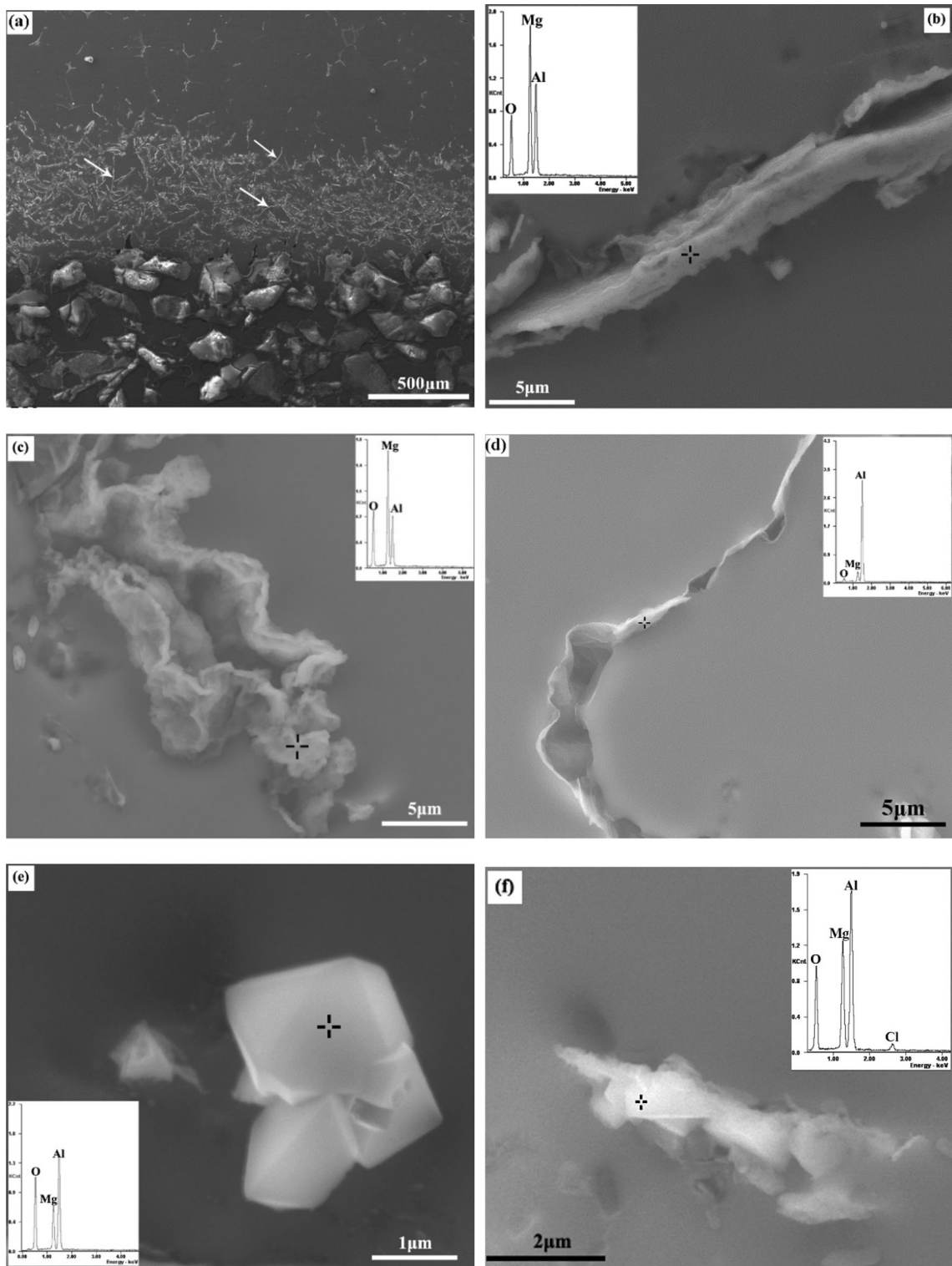
Fig. 5—SEM micrographs showing: (a) overview of collected inclusions, white arrows mark thick oxide films; (b) stringer like oxide film; (c) nodule-like oxide film; (d) curled oxide film; (e) cuboid oxide particle; (f) cuboid oxide nucleates upon oxide film. Inserts are result of spot EDS analysis performed at target symbol. Samples from Trial Nr. 6, 9, and 14, prepared by electrochemical polishing.

projected from within Al-MgO-Al_2O_3 triangle onto the Al_2O_3-$MgAl_2O_4$-MgO oxide line. The projection result is shown in Figure 6(b). It can be seen from Figure 6(b) the composition of examined oxide films all fall into

$MgAl_2O_4$-MgO line section, indicating oxide films are composed of MgO and $MgAl_2O_4$ phases. At higher melt temperature, no significant change of oxide film composition was observed.
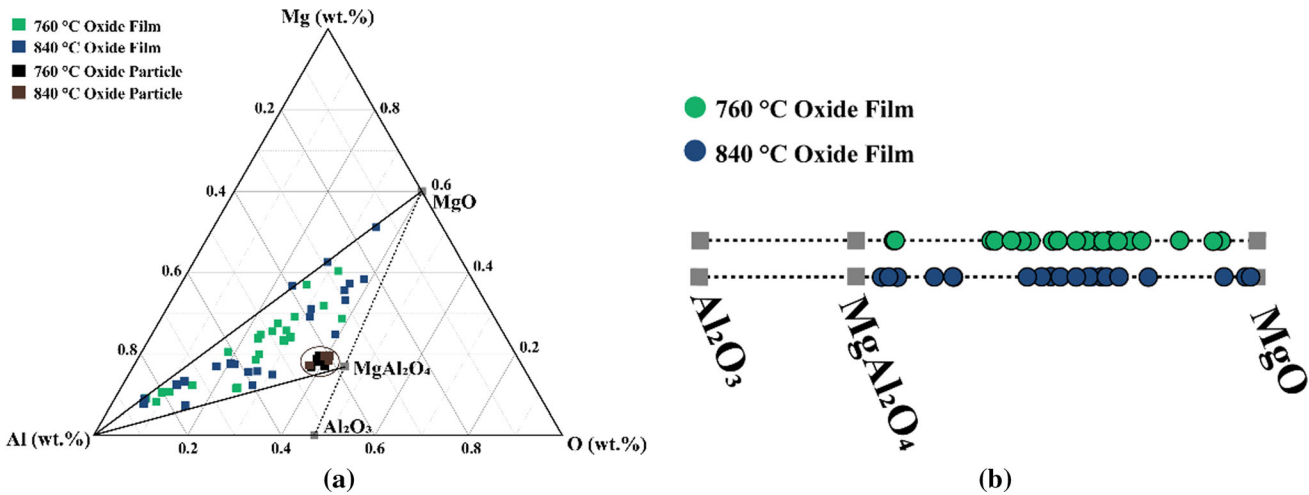
Fig. 6—EDS results pertaining to oxide film and cuboid oxide particle: (*a*) plot on Mg-Al-O ternary diagram; (*b*) composition projection on Al_2O_3-$MgAl_2O_4$-MgO line.

On the other hand, the composition of cuboid oxide particles lies in the vicinity of $MgAl_2O_4$ phase composition irrespective of melt holding temperature, as is marked by a circle in Figure 6(a). Given the similarity between the identified particles and the ones reported by Li *et al.*[51] with respect to morphology and composition, the identified cuboid oxide particles are believed to be $MgAl_2O_4$ phase. According to the study of Li *et al.*,[51] spinel particles were formed by thickening and breaking of thick oxide films. Our observation in Figure 5(f) indicates spinel particles can also be formed by the nucleation and growth of cuboid particles upon existed oxide film. Since composition of oxide film lies in between MgO and $MgAl_2O_4$, it can be seen as a potential nuclei for heterogeneous nucleation of $MgAl_2O_4$ particles. Note that the Cl peak in result of EDS analysis shown in Figure 5(f) was probably from the residue of electrolyte.

Spark spectrometer analysis of all samples taken from melt bath shortly before PoDFA sampling suggests ca. 4.5 wt pct Mg content of the alloy melt (Table III). The result suggests that Mg depletion did not happen. From this point of view our results are in line with the finding of Das *et al.*[26] and Wenz *et al.*[27] both of which identified $MgAl_2O_4$ as one of the typical oxidative products during remelting of Al-4 Mg alloys without depletion of Mg in the melt bath. However, both authors did not offer a sound explanation concerning formation of $MgAl_2O_4$ in melts with over 1.5 wt pct Mg content. At such high Mg concentration, $MgAl_2O_4$ was in fact not a thermodynamically favorable oxidative product.[23–25] In the present study, the authors try to explain this phenomenon from perspective of the dross layer. It has been well acknowledged in melting practices that after (re)-melting, a dross layer composed of mainly oxide films and entrapped metals exists in the vicinity of melt surface. The oxide films from the dross layer are more likely to be collected by PoDFA sampling since they have a higher chance to develop in size and quantity, by means of picking-up atmosphere oxygen during heating in liquid metal state. Within the dross

layer, suspended oxide films, if densely packed, can form "honeycomb" structure where metals are encapsulated separately in small units.[52] The dross structure can hinder the diffusion of Mg from melt bath towards the melt surface where Mg evaporates and oxidizes at a rapid rate.[53] Once the supply of Mg to dross layer is retarded, it is possible that after a certain time Mg content is depleted to a level of lower than 1.5 wt pct within the dross layer whilst Mg content keeps at 4.5 wt pct level in the melt bath. At extended heating cycle, which is the case for presented study, local depletion of Mg is prone to take place. As a result, formation of $MgAl_2O_4$ phase, either in form of oxide film or cuboid particles, becomes thermodynamically favorable within dross layer. Figure 7 shows schematically above proposed model.

Besides composition, oxides amount variation as function of heating rate was also investigated *via* quantitative PoDFA analysis. Results from Trial Nr. 1, 2, 6, 7, 9, 10, 14, and 15 were compiled and plot in Figure 8(a). Heating rate was calculated by dividing temperature change with time when the alloy was heated between solidus and liquidus temperature. A general trend of decrease in overall amount of oxides with increase of heating rate can be seen in Figure 8(a) with an exclusion of the 2.5 °C/minutes trial (equivalently 760 °C trial) which is highly deviated. Results shown in Figure 8(a) suggests heating rate during melting plays a significant role in determining oxide generation. The benefit of high heating rate was even able to offset the negative effect of high melt holding temperatures. This may be explained by the "first formed oxide" theory,[54] which stated the protective nature of the oxide formed on the melt surface upon melting decided following oxidation rate of the melt. At lower heating rate, a less coherent and more defective oxide films is expected to form on the melt surface after melting is complete, thus the melt can have a faster oxidation rate during melt holding. Figure 8(a) also gives the fraction of oxide films and cuboid in overall oxides. Despite the decrease of overall oxides amount in 3.7 and 5.5 °C/minutes trials
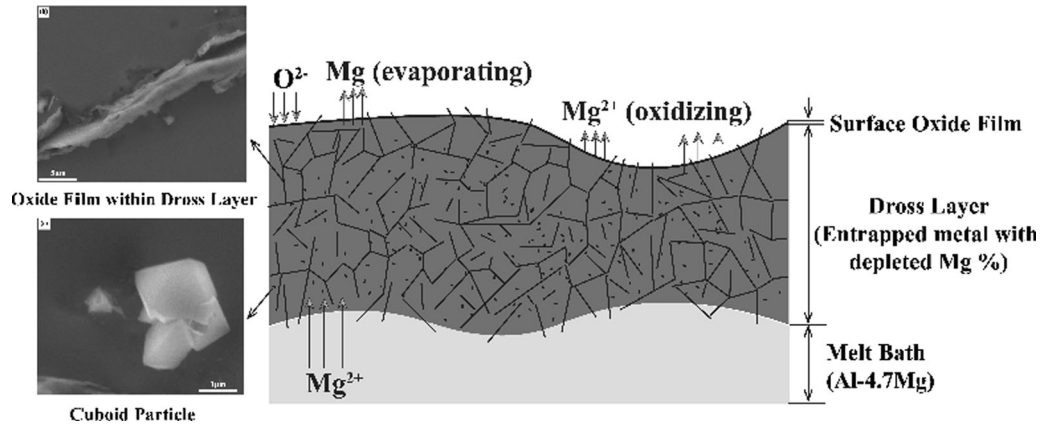
Fig. 7—Schematic of proposed model illustrating formation of MgAl$_2$O$_4$ phase within dross layer as a result of hindered Mg diffusion.
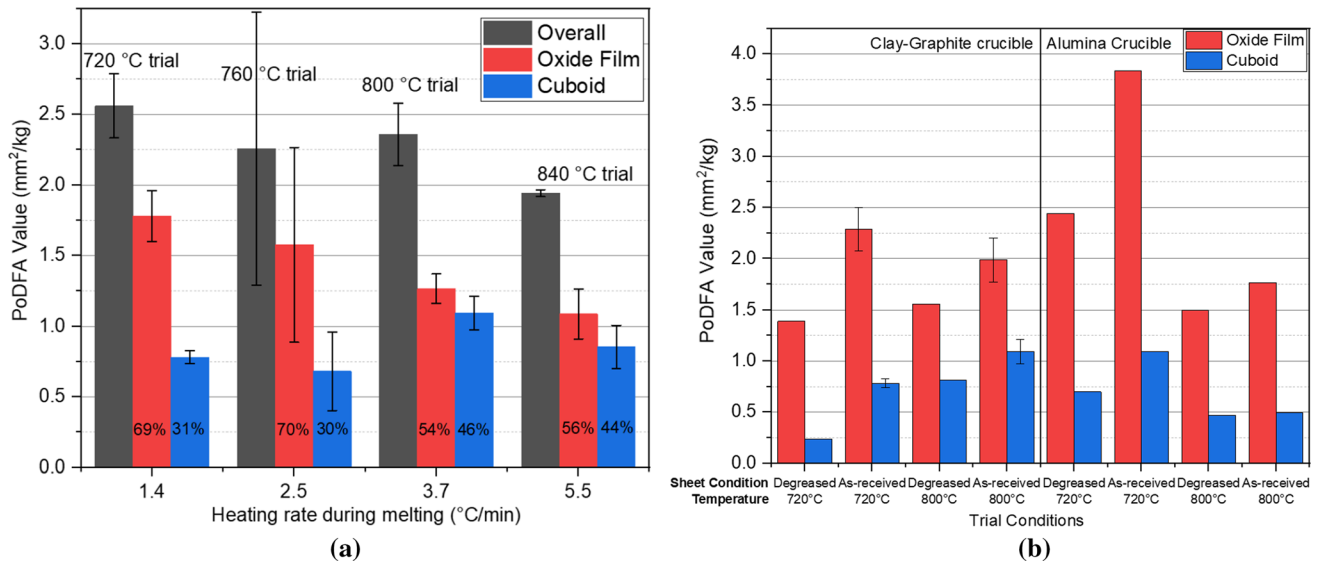
Fig. 8—Variation of oxide PoDFA values at different experimental parameters: (*a*) heating rate during melting; (*b*) sheet condition. Deviation of results are given when trials were repeated. Fraction of oxide films and cuboid particles were, respectively, given in inside data column of (a). Trial temperatures were given above data column in (a).

comparing with 1.4 and 2.5 °C/minutes trials, the ratio of cuboid amount to oxide films increased. The change can be attributed to direct oxidation of alloy (Reaction [2]) and transformation from oxide films to cuboid particles (Reaction [3] and [4]). At higher melt holding temperatures, rate of above mentioned reactions can be promoted.

$$1/2 \text{ Mg}[\text{Al}] + \text{Al}(l) + \text{O}_2(g) = 1/2\text{MgAl}_2\text{O}_4(s) \quad [2]$$

$$\text{Al}(l) + 2\text{MgO}(s) = 3/2 \text{ Mg}[\text{Al}] + 1/2\text{MgAl}_2\text{O}_4(s) \quad [3]$$

$$\text{MgO}(s) + \text{ Al}(l) + 3\text{O}_2(g) = \text{MgAl}_2\text{O}_4(s) \quad [4]$$
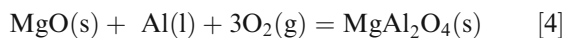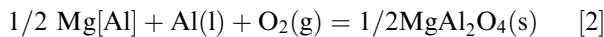
Figure 8(b) shows difference in oxides amount between trials using as-received sheet and trials using degreased sheet (Trial Nr. 1-5, 9-13). It demonstrates organic contaminations can significantly increase oxides amount and hence deteriorate the melt quality, despite the as-received sheet used in the presented study usually contains less than 1 wt pct organic contaminations. Reaction [5] proposed by Dittrich *et al.*[43] explains the oxide formation induced by organic contaminations.

$$\text{Al}(l) + 3/2\text{CO}_2(g) = 1/2\text{Al}_2\text{O}_3(s) + 3/2\text{CO}(g) \quad [5]$$

B. *Carbide (Al$_4$C$_3$)*

Figure 9 shows the SEM micrographs along with the EDS mapping of elemental C and O from PoDFA sample taken at 840 °C (Trial Nr. 15). The sample surface immediately after polishing [Figures 9(a) through (d)] and 10 days after being placed in ambient
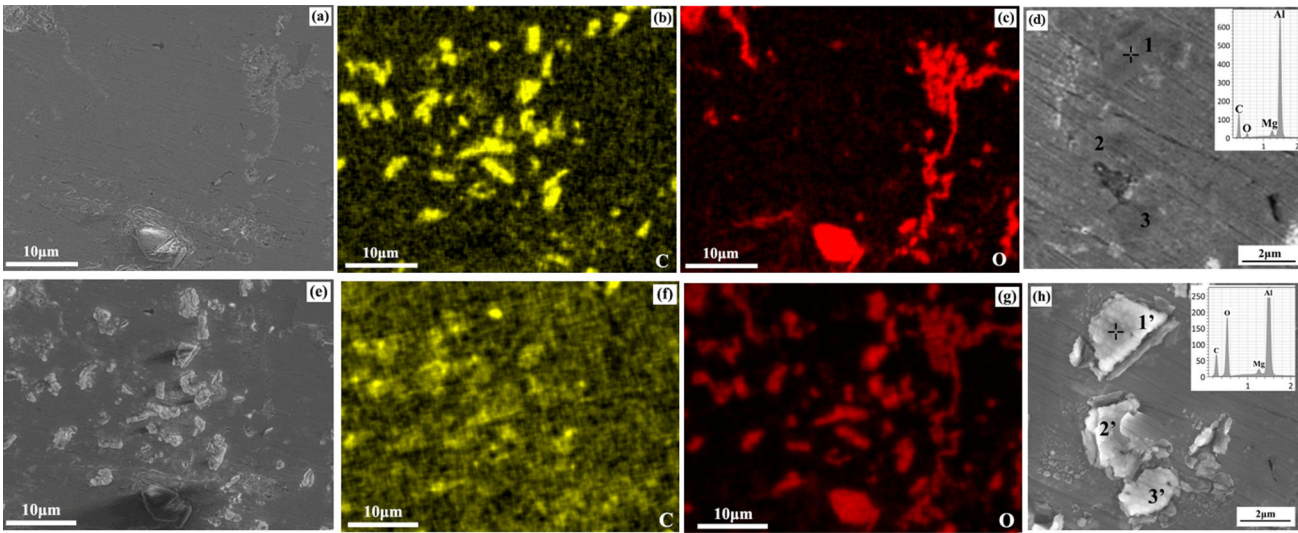
Fig. 9—SEM micrographs along with EDS mapping results showing sample surface: (*a*), (*b*), (*c*), and (*d*) immediately after polishing; (*e*), (*f*), (*g*), and (*h*) 10 days after being placed in ambient atmosphere. Spot 1, 2, and 3 in (*d*) mark Al_4C_3 particles before degradation, spot 1', 2' and 3' in (*h*) mark Al_4C_3 particles after degradation. Inserts in (*d*) and (*h*) are respectively EDS spot analysis results for spot 1 and 1'. Sample from Trial Nr. 15, prepared by mechanical polishing.

atmosphere [Figures 9(e) through (h)] were examined. It can be seen in Figures 9(a) through (c) that immediately after ethanol polishing, carbide (Al_4C_3) particles can only be revealed by elemental mapping of carbon. 10 days after polishing, particles with clear periphery appeared [Figure 9(e)] in the areas where C was initially detected [Figure 9(b)]. Moreover, at areas where carbide (Al_4C_3) particles appeared [Figure 9(e)] the detection of carbon element became difficult [Figure 9(f)], meanwhile oxygen element was evidently detected, as is shown in Figure 9(g). The observation suggested a degradation of carbide (Al_4C_3)[40] through Reaction [6].

$$Al_4C_3(s) + 12H_2O(g) = 3CH_4(g) + 4Al(OH)_3(s) \quad [6]$$
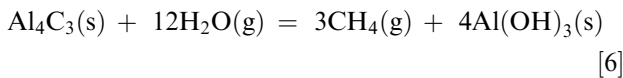
A close-up of Al_4C_3 particles observation before and after degradation is given in Figures 9(d) and (h) along with EDS analysis. The low Mg peak appeared in the spectrum might be attributed to the electron signal collected from Al-Mg alloy matrix behind as the Al_4C_3 particles whose thickness perpendicular to measured surface are mostly less than 1.5 μm. When hydrolysis reaction (Reaction [6]) took place, the bonding between polyhedral Al_4C_3 particles and alloy matrix dramatically deteriorated and a peripheral gap was observed at the interface. The gap enables an easy distinguish between the Al_4C_3 particles from other kinds of non-metallic inclusions present in Al-Mg alloys. Dimension measurement suggest Al_4C_3 particles in cuboid/polyhedral form have a size ranging from 0.5 to 7 μm in samples from Trial Nr. 7, 10, 15. A detailed carbide particle size distribution will be presented in sub-chapter III-D.

Figure 10 shows Al_4C_3 amount variation as a function of temperature. It is shown in Figure 10(a) that the overall amount of Al_4C_3 formed, using degreased sheet, was always less than Al_4C_3 formed using as-received sheet, irrespectively of crucibles that were used. The

results indicate, besides dissolution–precipitation formation mechanism[35] which is described in Reaction [7], Al_4C_3 can be formed through exothermic Reaction [8] or [9].[43,44] The exothermic reactions may contribute separately to overall amount of Al_4C_3 formation. This finding supports the proposal of Steglich *et al.*[44] and Dittrich *et al.*,[43] that remelting scraps with organic contaminations can lead to formation of Al_4C_3.

$$4Al(l) + 3C[Al] = Al_4C_3(s) \quad [7]$$

$$Al(l) + 3/4C(s) = 1/4Al_4C_3(s) \quad [8]$$

$$Al(l) + 3/4CH_4(g) = 1/4 Al_4C_3(s) + H_2(g) \quad [9]$$
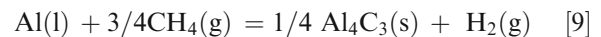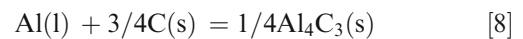
Figure 10(a) also shows the influence of crucible materials on Al_4C_3 formation. Irrespective of sheet conditions, when temperature went beyond 760 °C, Al_4C_3 overall amount increased remarkably only when clay-graphite crucible was used. A comparison between clay-graphite crucible (square symbol) and alumina crucible curve (downwards triangle symbol) suggests, at temperature over 760 °C, Al_4C_3 sourced from the dissolved carbon (Reaction [7]) contributes more significantly to Al_4C_3 formation than organic contaminations (Reaction [8] or Reaction [9]) which adheres on sheet used in the present study.

Based on plot given in Figure 10(a), the averaged amount of Al_4C_3 formed from exothermic reactions can be tentatively calculated by subtracting Al_4C_3 PoDFA values of degreased sheet from Al_4C_3 PoDFA values of as-received sheet. The calculation was made for both two types of crucibles and averaged value is given in dashed line in Figure 10(a). With the obtained average value, the amount of Al_4C_3 formed from dissolved
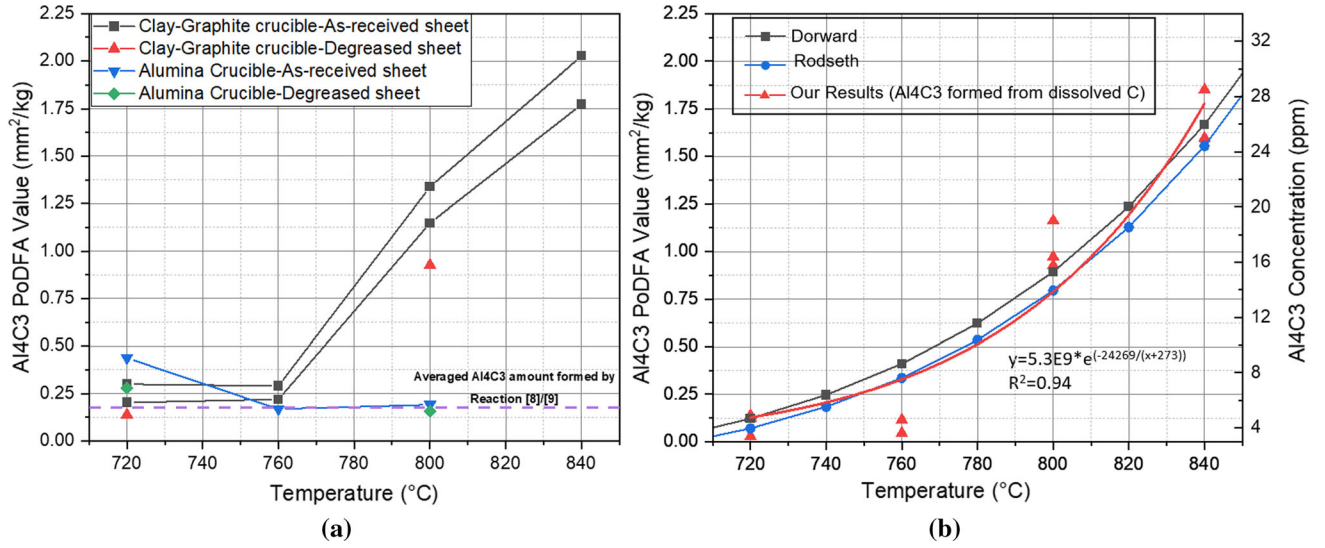
Fig. 10—Al_4C_3 amount (PoDFA value) variation as a function of temperature: (*a*) overall Al_4C_3 amount; (*b*) Al_4C_3 amount that formed through dissolved carbon in comparison with literature data, dual axis. Dashed line in (a) indicates tentatively calculated Al_4C_3 value formed *via* Reaction [8]/[9].

carbon as a function of temperature can be calculated and the result is plotted Figure 10(b) with left-hand-side axis showing Al_4C_3 PoDFA value. Literature results are also given in Figure 10(b) with right-hand-side axis showing Al_4C_3 mass fraction. Since our results agree with the GC analytics in terms of exponential feature, an exponential fit was made and the result is insert in Figure 10(b) and given in Eq. [10],

$$P_{Al4C3} = 5.3 \times 10^9 \times e^{\frac{-24269}{T}} \quad [10]$$

where P_{Al4C3} [mm^2/kg] is the carbide amount (from dissolved carbon) measured by PoDFA method. T [K] is corresponding melt temperature. On the other hand, the mass fraction of Al_4C_3 (W_{Al4C3} [ppm]) sourced from dissolved carbon as a function of melt temperature T [K] was given by Rodseth:[36]

$$W_{Al4C3} = 8.31 \times 10^7 \times e^{\frac{-16742}{T}} \quad [11]$$

Assuming all precipitated Al_4C_3 particles have been collected during the PoDFA filtration, by combining Eqs. [10] and [11], Eq. [12] can be obtained:

$$W_{Al4C3} = 16 \cdot (P_{Al4C3})^{0.69} \quad [12]$$

The above equation offers a way to translate Al_4C_3 PoDFA value [mm^2/kg] into its mass fraction [ppm] in the melt, the former of which is often seen as an index for inclusion amount instead of its real concentration.

C. Borides

BSE (Backscattered Electrons) examination of boride was made using PoDFA samples from Trial Nr. 7, 10 and 15. Representative micrographs are shown in Figure 11. Boride particles are much finer in size

(sub-micro) than oxides and carbide particles and is with a polyhedral/rod shape. EDS elemental analysis indicates the borides are composed of Ti, V, and B. Al element may also be contained in the boride phase upon inoculation of TiB_2 and the follow-up remelting-holding practice, despite EDS analysis can not rigorously confirm its presence. Nevertheless based on previous literatures evidences,[55,56] it is proposed the boride phase shown in Figure 11(a) is possibly a solid solution of (Ti, V, Al)B_2. It is interesting to find most boride particles and Al_4C_3 particles co-exist in the same region as patch of clusters. During solidification, those particles were possibly pushed towards the last solidified region and formed cluster there. Dimension measurement suggest boride particles in cuboid/rod form have a size ranging from 0.2 to 2.0 μm in samples obtained from Trial Nr. 7, 10, 15. A detailed boride particle size distribution will be presented in sub-chapter III-D.

Based on obtained mass fraction of Al_4C_3 particles. The relation between boride PoDFA value and its mass fraction in the melt can also be established. We firstly apply Eq. [1] (Sub-chapter II-C) respectively for Al_4C_3 and boride inclusion in the same PoDFA sample:

$$P_{Al4C3} = \frac{A_{Al4C3}}{m_{fil}} \cdot \frac{L_{noc}}{L_{mec}} \quad [13]$$

$$P_{Boride} = \frac{A_{Boride}}{m_{fil}} \cdot \frac{L_{noc}}{L_{mec}} \quad [14]$$

where m_{fil} [kg] is filtrated melt mass, L_{noc} [mm] is nominal chord length, L_{mec} [mm] is measured chord length. A_{Al4C3} and A_{Boride} [mm^2] is respectively the area of Al_4C_3 and boride counted on the polished
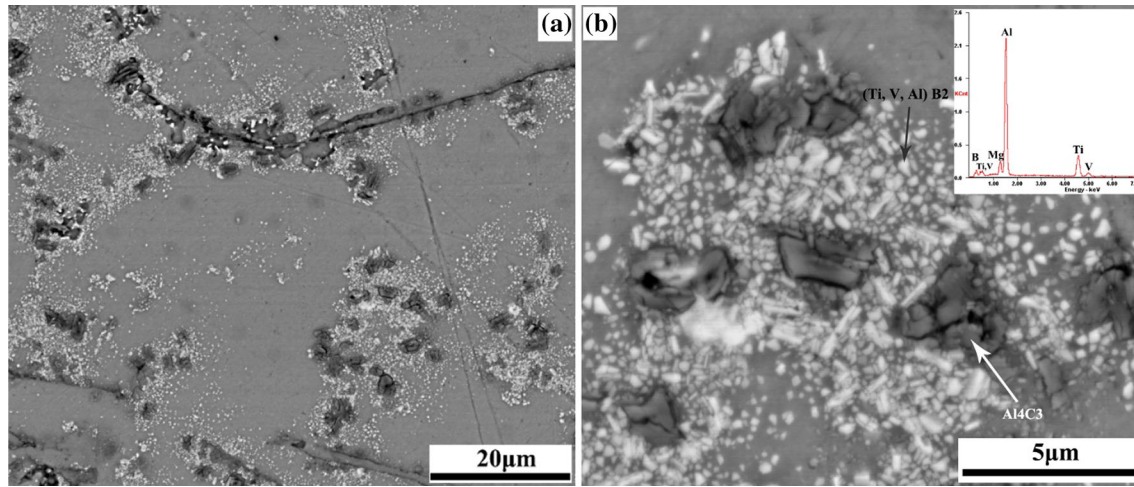
Fig. 11—Distribution and morphology of boride and Al_4C_3: (a) low magnification view field; (b) high magnification field. Black arrow in (b) marks $(Ti, V, Al)B_2$ particle, white arrows in (b) mark Al_4C_3 (hydrolyzed). Sample from Trial Nr. 10 prepared by mechanical polishing. Insert of (b) is result of spot EDS analysis of boride.
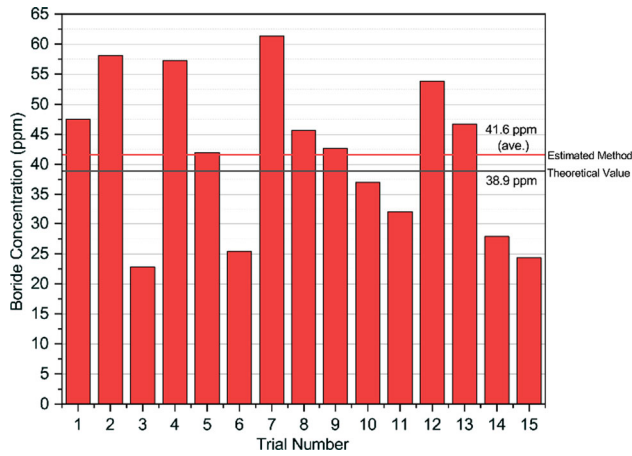
Fig. 12—Boride mass fraction estimated based on proposed translation method. Results from all 15 trials.

surface *via* PoDFA grid method. For the same PoDFA sample, m_{fil} [kg], L_{noc}[mm], and L_{mec} [mm] are all constants. Therefore By dividing Eq. [13] with Eq. [14], and Eq. [15] can be obtained:

$$\frac{P_{Al4C3}}{P_{Boride}} = \frac{A_{Al4C3}}{A_{Boride}} \qquad [15]$$

According to Delesse stereological principle,[57] in the same PoDFA sample with both Al_4C_3 and boride collected (*e.g.*, Figure 11), Eq. [16] can be written:

$$\frac{V_{Al4C3}}{V_{Boride}} = \frac{A_{Al4C3}}{A_{Boride}} \qquad [16]$$

where V_{Al4C3} and V_{Boride} [mm^3] respectively means the volume of Al_4C_3 and boride collected above the filter. A combination of Eqs. [15] and [16] leads to:

$$\frac{V_{Al4C3}}{V_{Boride}} = \frac{P_{Al4C3}}{P_{Boride}} \qquad [17]$$

On the left hand side of Eq. [17], by transferring the volume of respective inclusion into its mass using corresponded density constant, Eq. [18] can be written:

$$\frac{M_{Al4C3}}{M_{Boride}} = \frac{\rho_{Al4C3}}{\rho_{Boride}} \cdot \frac{P_{Al4C3}}{P_{Boride}} \qquad [18]$$

where M_{Al4C3} and M_{Boride} [kg] means respectively mass of Al_4C_3 and boride inclusion collected above the filter. ρ_{Al4C3} and ρ_{Boride} [kg/m^3] means respectively density of Al_4C_3 and boride. Assuming all inclusions have been collected during the filtration, the mass fraction of Al_4C_3/boride in the melt can be obtained by dividing the mass of collected particles (Al_4C_3/boride) with mass of filtrated metal (m_{fil} [kg]). Since m_{fil} [kg] is the same for Al_4C_3 and boride particles in each filtration trial, the ratio of collected mass of Al_4C_3 particle to boride particle equals to ratio of Al_4C_3 mass fraction to boride mass fraction. Hence one may readily write Eq. [19]:

$$\frac{W_{Al4C3}}{W_{Boride}} = \frac{\rho_{Al4C3}}{\rho_{Boride}} \cdot \frac{P_{Al4C3}}{P_{Boride}} \qquad [19]$$

where W_{Al4C3} and W_{Boride} [ppm] means respectively mass fraction of Al_4C_3 and boride inclusion in the melt. Substituting Eq. [12]. along with density constant of Al_4C_3 and boride into Eq. [19], mass fraction of boride can be obtained by:

$$W_{Boride} = 31 \cdot \frac{P_{Boride}}{(P_{Al4C3})^{0.31}} \qquad [20]$$

Application of Eq. [20] in PoDFA results obtained from all 15 trials lead to a diagram of boride mass fraction in the melt, as is shown in Figure 12. Our estimation method predicted on average 42 ppm boride particle existed in the melt, which is within a deviation of 10 pct to theoretical value 39 ppm predicted by Quested.[58] This result demonstrates that the proposed estimation method is effective in gaining general information of inclusion concentration in the melt, which is so far still very much experience based.

It is worth emphasizing that Eq. [19] can be generalized into a formula given in Eq. [21]

Table V. Type, Size, Morphology, and Concentration of NMIs Present in As-Remelted 5000 Alloy Melt

Type of NMIs	Mg-Al-O Film	$MgAl_2O_4$	Al_4C_3	Boride
Size	Length 15–200 μm, Thickness 0.1–3 μm	0.5–3 μm	0.5–7 μm	0.2–2 μm
Morphology	Stringer/Skin/nodule	Cuboid	Polyhedron	polyhedral /Rod
Concentration	24–100 ppm	11–35 ppm	4–26 ppm	23–61 ppm
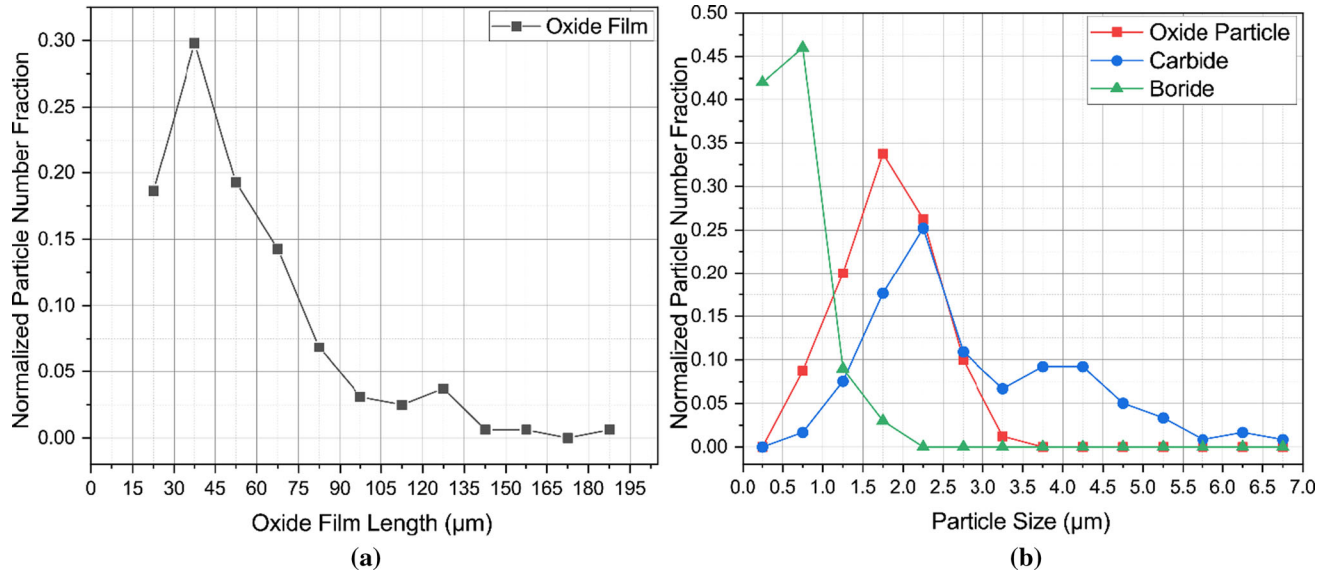
Fig. 13—Non-metallic inclusions size distribution of: (*a*) oxide film; (*b*) oxide, carbide, and boride particles. For oxide inclusions the size quantification was conducted on samples from Trial Nr. 6, 9, and 14. For carbide, and boride it is from Trial 7, 10, and 15.

$$\frac{W_b}{W_t} = \frac{\rho_b}{\rho_t} \cdot \frac{P_b}{P_t} \qquad [21]$$

where W_b and W_t [ppm] is respectively mass fraction of benchmarked inclusion and target inclusion. ρ_b and ρ_t [kg/m^3] is respectively density of benchmarked inclusion and target inclusion. P_b and P_t [mm^2/kg] is respectively PoDFA value of benchmarked inclusion and target inclusion. Eq. [21] shall be helpful for translating PoDFA value into corresponded mass fraction for an arbitrary type of target inclusion. Nevertheless, for using Eq. [21], a prerequisite is to have a mass fraction value from a benchmarked inclusion. In our study, the benchmarked inclusion is Al_4C_3 whose mass fraction value can be calculated based on in Eq. [12]. In other scenarios where Al_4C_3 amount is too less to be accurately counted *via* PoDFA method, it maybe more appropriate to resort to another type of benchmarking inclusion whose mass fraction can be reliably measured or estimated.

D. *Overview of All Inclusions*

Based on above findings, the type, size, and morphology of NMIs present in as-remelted 5000 alloy melt is summarized in Table V. Inclusion size distribution for each type of NMIs is summarized in Figures 13(a) and

(b). Note that the normalized particle number fraction within each size sub-range (*e.g.*, 30 to 45 μm) is represented by a single data point.

Analogously to the estimation of boride mass fraction, the formula used to translate PoDFA values of oxides to their mass fraction in the melt was derived and given in:

$$W_{oxide} = 25 \cdot \frac{P_{oxide}}{(P_{Al4C3})^{0.31}} \qquad [22]$$

Based on Eqs. [12, 20], and [22]. NMIs concentration in characterized in all 15 trials were estimated on single type inclusion basis and results are given in Table V and plotted in Figure 14.

Table V along with diagram shown in Figures 13 and 14 gives boundary conditions of NMIs feature in secondary as-remelted 5000 alloy. Figures 13(a) and (b) shows that length of oxide films spans over a much longer range comparing with other particle shape inclusions. Meanwhile the average size of particle shape inclusions increases from boride-type, to oxide-type, and further to carbide type. It can be seen from Figure 14, oxides (incl. film and cuboid) account for majority of the inclusions and their mass fraction spans over a wide range whilst carbide account only for minority of inclusions.
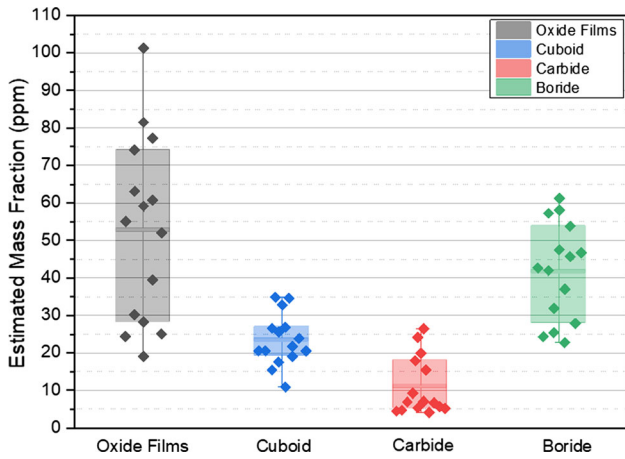
Fig. 14—Non-metallic inclusions mass fraction estimated based on proposed translation method. Results from all 15 trials. Horizontal thin stick gives the average value.

IV. CONCLUSIONS

Non-metallic inclusions (NMIs) formed during remelting of AA-5182 Al-Mg sheet at elevated temperatures (720 °C to 840 °C) in clay-graphite and alumina crucible were concentrated *via* a PoDFA set-up and characterized extensively. The findings are summarized as follows:

- Typical oxides in film and cuboid particle form were identified with different compositions. Oxide particles were observed to nucleate upon oxide film. A "dross layer" theory was proposed to explain formation of $MgAl_2O_4$ under non-depleted Mg condition.
- The overall amount of oxides declined: (1) with increase of heating rate during melting; (2) with degreasing treatment of sheet. The finding implies the importance of rapid melting and decoating treatment.
- Identification criterion of aluminum carbide (Al_4C_3) under electron microscope is established.
- First hand evidence confirms remelting scraps with organic contaminations can lead to an increased amount of carbide formation. The carbon-containing refractory material contributes more significantly than organic contaminations on the Al_4C_3 formation at melt temperatures over 760 °C.
- Formulas were derived to enable translation of NMIs PoDFA value [mm²/kg] into their mass fraction [ppm] in the melt.

$$W_{Al4C3} = 16 \cdot (P_{Al4C3})^{0.69}$$

$$W_{Boride} = 31 \cdot \frac{P_{Boride}}{(P_{Al4C3})^{0.31}}$$

$$W_{oxide} = 25 \cdot \frac{P_{oxide}}{(P_{Al4C3})^{0.31}}$$

- Reference information of NMIs in as-remelted 5000 Al-Mg was provided. Such information may help better prescribe inclusions removal processes in the future.

CONFLICT OF INTEREST

The authors declare no conflicts of interest.

ABBREVIATIONS

A   Area of inclusion collected above filter, mm²
L   Chord length of filter, mm
m   Filtrated mass, kg
M   Mass of inclusion collected above filter, kg
P   PoDFA value of inclusion, mm²/kg
T   Temperature, K
V   Volume of inclusion collected above filter, mm³
W   Mass fraction of inclusion in the melt, ppm
ρ Density, kg/m³

REFERENCES

1. D. Raabe, D. Ponge, P.J. Uggowitzer, M. Roscher, M. Paolantonio, C. Liu, H. Antrekowitsch, E. Kozeschnik, D. Seidmann, B. Gault, F. De Geuser, A. Deschamps, C. Hutchinson, C. Liu, Z. Li, P. Prangnell, J. Robson, P. Shanthraj, S. Vakili, C. Sinclair, L. Bourgeois, and S. Pogatscher: *Prog. Mater. Sci.*, 2022, https://doi.org/10.1016/j.pmatsci.2022.100947.
2. C. Tian, J. Law, J. Van der Touw, M. Murray, J.Y. Yao, D. Graham, and D. St. John: *J. Mater. Process. Technol.*, 2002, vol. 122, pp. 82–93.
3. C.J. Simensen: *Aluminium*, 1980, vol. 56, pp. 335–40.
4. S. Vantadori, C. Ronchei, D. Scorza, A. Zanichelli, L.C. Araújo, and J.A. Araújo: *Int. J. Fatigue*, 2022, vol. 154, p. 106553.
5. M. Rezaul Karim, K. Kadau, S. Narasimhachary, F. Radaelli, C. Amann, K. Dayal, S. Silling, and T.C. Germann: *Int. J. Fatigue*, 2021, vol. 153, p. 106475.
6. C. Capurro, R. Boeri, and C. Cicutti: *Steel Res. Int.*, 2022, vol. 93, pp. 1–1.
7. S. Imashuku and K. Wagatsuma: *ISIJ Int.*, 2022, vol. 62, pp. 811–20.
8. H.V. Atkinson and G. Shi: *Prog. Mater. Sci.*, 2003, vol. 48, pp. 457–520.
9. W. Chen, L. Zhang, Q. Ren, Q. Wang, X. Cai, Y. Ren, and W. Yang: *Metall. Mater Trans. B Process Metall. Mater. Process. Sci.*, 2021, vol. 52, pp. 3497–514.
10. R.I.L. Guthrie and M. Li: *Metall. Mater Trans. B Process Metall. Mater. Process. Sci.*, 2001, vol. 32, pp. 1081–93.

11. M. Badowski, T. Dang, N. Towsey, D. Krings, and K. Hoffmann: *TMS light meetings*, Springer, Cham, 2018, pp. 847–54.
12. D. Neff: *Die Cast. Eng.*, 2004, vol. 48, pp. 24–26.
13. M. Gökelma, D. Latacz, and B. Friedrich: *Open J. Met.*, 2016, vol. 06, pp. 13–24.
14. M.M. Jaradeh and T. Carlberg: *Metall. Mater Trans. B Process Metall. Mater. Process. Sci.*, 2011, vol. 42, pp. 121–32.
15. ABB Inc., Brochure-PoDFA the complete solution for inclusion measurement, inclusion identification and quantification analysis. https://search.abb.com/library/Download.aspx?DocumentID=PB%2FPoDFA-EN&LanguageCode=en&DocumentPartId=&Action=Launch&DocumentRevisionId=A. Accessed 8 Sept 2022.
16. E. Haugland, Ph.D. thesis, The Norwegian University of Science and Technology (1998).
17. L. Liu and F.H. Samuel: *J. Mater. Sci.*, 1997, vol. 32, pp. 5901–25.
18. F.H. Samuel, P. Ouellet, and A. Simard: *Int. J. Cast Met. Res.*, 1999, vol. 12, pp. 17–33.
19. K. Haberl, P. Schumacher, G. Geier, and B. Stauder: *Metall. Mater Trans. B Process Metall. Mater. Process. Sci.*, 2009, vol. 40, pp. 812–21.
20. Y. Wang, H.T. Li, Z. Fan, and G. Scamans: *Mater. Sci. Forum*, 2013, vol. 765, pp. 220–24.
21. K. LaPointe, S. Bao, and A. Kvithyld: *Metall. Mater Trans. B Process Metall. Mater. Process. Sci.*, 2015, vol. 46, pp. 1326–42.
22. N. Smith, A. Kvithyld, and G. Tranell: *Metall. Mater Trans. B Process Metall. Mater. Process. Sci.*, 2018, vol. 49, pp. 2846–57.
23. M.P. Silva, Ph.D. thesis, Brunel, The University of West London (1987).
24. K. Surla, F. Valdivieso, M. Pijolat, M. Soustelle, and M. Prin: *Solid State Ion.*, 2001, vol. 143, pp. 355–65.
25. A.D. McLeod and C.M. Gabryel: *Metall. Trans. A*, 1992, vol. 23, pp. 1279–83.
26. S.K. Das, Reduction of oxidative melt loss of aluminum and its alloys. https://www.osti.gov/servlets/purl/877410. Accessed 8 Sept 2022.
27. D.A. Wenz: *TMS Light Met.*, Metallurgical Society of AIME, New York, 1979, pp. 771–80.
28. I. Haginoya and T. Fukusako: *Trans. Jpn. Inst. Met.*, 1983, vol. 24, pp. 613–19.
29. C.N. Cochran, D.L. Belitskus, and D.L. Kinosz: *Metall. Trans. B*, 1977, vol. 8, pp. 323–32.
30. H.T. Li, Ph.D. thesis, Brunel University (2011).
31. D.J. Field, G.M. Scamans, and E.P. Butler: *Metall. Trans. A Phys. Metall. Mater. Sci.*, 1987, vol. 18, pp. 463–72.
32. J.A.S. Tenório and D.C.R. Espinosa: *Oxid. Met.*, 2000, vol. 53, pp. 361–73.
33. L.N.W. Damoah, L. Zhang, and N.F. Adegboyega: *TMS Light Met.*, Minerals, Metals and Materials Society, Warrendale, PA, 2010, pp. 773–78.
34. K.L. More, P.F. Tortorelli, L.R. Walker, J. Hryn, and G. Krumdick: *Mater. High Temp.*, 2003, vol. 20, pp. 453–60.
35. R.C. Dorward: *Aluminium*, 1973, vol. 10, pp. 686–89.
36. J. Rodseth, B. Rasch, O. Lund, and J. Thonstad: *TMS Light Met.*, TMS, the Minerals, Metals & Materials Society, Warrendale, PA, 2002, pp. 883–88.
37. M. Gökelma, T. Storm Aarnæs, J. Maier, B. Friedrich, and G. Tranell: *TMS Light Met.*, 2019, pp. 1033–039. https://doi.org/10.1007/978-3-030-05864-7_126.
38. C.J. Simensen: Fresenius' Zeitschrift für Anal. *Chemie*, 1978, vol. 292, pp. 207–12.
39. J.P. Martin, G. Dube, D. Frayce, and R. Guthrie: *TMS Light Met.*, Metallurgical Society. Warrendale, PA, 1988, pp. 115–25.
40. M. Gökelma, T. Storm Aarnæs, J. Maier, M.F. Renkel, K.E. Ekstrøm, B. Friedrich, and G. Tranell: *Metall. Mater Trans. B Process Metall. Mater. Process. Sci.*, 2021, vol. 52, pp. 743–54.
41. C.J. Simensen: *Metall. Trans. A*, 1989, vol. 20A, p. 191.
42. B. Jaroni, K. Gisbertz, G. Rombach, and B. Friedrich: *Aluminium*, 2011, pp. 2–5. https://www.metallurgie.rwth-aachen.de/pdf/publications/eac_rwth_290911_id_7792.pdf.
43. R. Dittrich, B. Friedrich, G. Rombach, J. Steglich, and A. Pichat: *TMS Light Met.*, 2017, vol. 2, pp. 1457–64.
44. J. Steglich, R. Dittrich, G. Rombach, M. Rosefort, B. Friedrich, and A. Pichat: *TMS Light Met.*, 2017, pp. 1105–113. https://doi.org/10.1007/978-3-319-51541-0_133.
45. J.K. Park and J.P. Lucas: *Scr. Mater.*, 1997, vol. 37, pp. 511–16.
46. Z. Fan, Y. Wang, Y. Zhang, T. Qin, X.R. Zhou, G.E. Thompson, T. Pennycook, and T. Hashimoto: *Acta Mater.*, 2015, vol. 84, pp. 292–304.
47. X. Wang and Q. Han: *TMS Light Met.*, 2016, pp. 189–93. https://doi.org/10.1007/978-3-319-48251-4_32.
48. J. Yang, S. Bao, S. Akhtar, U. Tundal, S. Tjøtta, and Y. Li: *Metall. Mater Trans. B Process Metall. Mater. Process. Sci.*, 2021, vol. 52, pp. 3946–60.
49. P.V. Evens, P.G. Enright, and R.A. Ricks: *TMS Light Met.*, 2018, pp. 839–46. https://doi.org/10.1007/978-3-319-72284-9_109.
50. W.J.M. Tegart: *The electrolytic and chemical polishing of metals*, Pergamon Press, London, 1956.
51. H.T. Li, Y. Wang, and Z. Fan: *Acta Mater.*, 2012, vol. 60, pp. 1528–37.
52. W. Stevens, G. Riverin, V. Goutieres, and J. Fortin: *TMS Light Met.*, 2003, vol. 2, pp. 801–08.
53. C. Lea and C. Molinari: *J. Mater. Sci.*, 1984, vol. 19, pp. 2336–52.
54. S.A. Impey, Ph.D. Thesis, Cranfield Institute of Technology (1989).
55. X. Wang, Z. Liu, W. Dai, and Q. Han: *Metall. Mater Trans. B Process Metall. Mater. Process. Sci.*, 2015, vol. 46, pp. 1620–25.
56. A. Khaliq, A.S. Alghamdi, W. Rajhi, T. Subhani, M. Ramadan, K.S.A. Halim, and M. Qian: *Metall. Mater Trans. B Process Metall. Mater. Process. Sci.*, 2021, vol. 52, pp. 3130–41.
57. V. Howard and M. Reed: *Unbiased stereology: three-dimensional measurement in microscopy*, Garland Science, New York, 2004.
58. T.E. Quested and A.L. Greer: *Acta Mater.*, 2004, vol. 52, pp. 3859–68.